Predicting energy harvesting performance of a random nonlinear dielectric elastomer pendulum

Peng Fan[1,2], Liangquan Zhu[2], Zicai Zhu[2], Hualing Chen[2], and Hong Hu[1]

[1]*Institute of Textile and Clothing, The Hong Kong Polytechnic University, Hong Kong, China*

[2] *School of Mechanical Engineering, Xi'an Jiaotong University, Xi'an, China*

(a) Corresponding author. Email: hu.hong@polyu.edu.hk

Abstract

This paper investigates the energy harvesting (EH) performance of a nonlinear dielectric elastomer (DE) pendulum under the random excitation. The DE pendulum that can convert the vibration energy into the electrical energy consists of a DE membrane with a mass, which is similar to a spring pendulum. A dynamic analysis model of the nonlinear electromechanical coupling behavior of the DE pendulum under the random excitation is developed. A prototype of the DE pendulum is designed to evaluate the developed dynamic model, which shows the good agreement. On this basis, the stochastic dynamic behavior of the DE pendulum is analyzed by changing the intensity, the power spectrum density, and the upper limiting frequency of the random excitation. The EH performance of the DE pendulum under the random excitation is also studied for diverse system parameters, including ~~such as~~ the length of the DE membrane, the mass of the DE pendulum, and the load resistance. The results can help provide a guidance for designing the DE pendulum in the random vibration environment ~~so as~~ to improve the EH performance.

1. Introduction

In view of the depletion of conventional fossil fuel and global warming, the exploration and exploitation of renewable and green energy have become urgent [1]. Vibration, as a type of renewable energy source, has been an attractive target for energy harvesting (EH) due to its abundance in ambient environment. Vibration EH, namely, converting the vibration energy into the electrical energy, can be realized through piezoelectric generators [2,3], electromagnetic generators [4,5], and dielectric elastomer generators (DEGs) [6,7], which can be used as power sources for a wide range of promising applications, such as automobiles [8,9], wearable electronic devices [10-12], and biomedicine [13,14]. Experimental study has shown that the DEG can generate ~~the~~ a power density of 2.8mW/mm^3 [15], which is much higher than that in piezoelectric and electromagnetic generators [16,17]. In addition,

dielectric elastomers (DEs) possess other intrinsic advantages, such as large deformation, fast response, low cost, and flexibility [18-20]. On account of this, DEs have attracted much research attention ~~so as to be used~~ for the use not only in EH [21,22] but also as actuators [23,24], sensors [25,26], and soft robotics [27,28].

A DEG consists of a soft elastomeric membrane sandwiched between two compliant electrodes. A typical EH cycle of DEGs is implemented as follows. When a pre-stretched and pre-charged DEG is contracted under the open circuit condition, the voltage between the electrodes is boosted, which accomplishes the charge transfer from a low potential to a high potential, and then, the charge at the high potential is harvested before the next cycle begins. Utilizing the typical EH cycle, Pelrine et al. first proposed a DE-based energy harvester embedded into a heel of a shoe, which could achieve ~~the~~ an energy density of 0.4 J/g [29]. Then, they developed a theoretical analysis model to analyze and predict its electromechanical properties ~~of the DE~~ ~~its theoretical analysis model is developed~~ [30,31]. With the deepening of the research in the DE, its applications were continuously increasing. To perform as an actuator or a generator, the DE was often subject to transient, time-dependent forces and voltages, in which the rate-dependent electromechanical behavior was discovered [32]. To describe the electromechanical behavior, Suo' group [22,33] developed ~~the~~ a dissipative model of DEs by considering the material viscosity and current leakage. ~~On this basis,~~ Based on this model, they also investigated the effect of DE material properties [22,34-36], geometrical parameters of DEGs [22,37], and external stimulus [35-40] on the EH performance of membranous DEGs ~~was also investigated~~. ~~In addition,~~ Some researchers also focused on the development and EH performance evaluation of the DE-based EH devices such as ocean wave generators [41,42] and vibration EH devices [6,43-46]. It could be noticed that most of work on DE-based EH were conducted with harmonic excitation inputs or uniform velocity excitation inputs. This means that the studies on membranous DEGs or DE-based EH devices mainly focused on converting the harmonic motions or uniform velocity reciprocating motions into the electrical energy, while the DE-based EH from the random excitation that can often be found in ambient environment is still relatively unexplored. Therefore, it is necessary to further investigate the EH performance of DEGs under random excitations. Thomson et al. investigated the EH performance of the vibro-impact DEG under the random excitation [45]. The research work in this paper is based on the DE pendulum reported in our previous works [6], which consists of a DE membrane with a mass. When the DE pendulum is externally excited, the DE membrane can be repeatedly stretched and relaxed, ~~which~~ converting the vibration energy into the electrical energy. In this paper, the dynamic behavior and the EH performance of the

DE pendulum under the random excitation are investigated ~~so as to~~ which can be serve as ~~the~~ a guidance for designing the DE pendulum in the practical applications.

The dynamic analysis model of the DE pendulum under the random excitation is developed in Section 2 of this paper. In Section 3, the developed dynamic model is verified by experimental results. The dynamic behavior of the DE pendulum is analyzed under the random excitation in Section 4. Section 5 investigates the EH performance of the DE pendulum under the random excitation for different system parameters, ~~such as~~ including the length of the DE membrane, the mass of the DE pendulum, and the load resistance. Conclusions are summarized in Section 6.

2. Dynamic analysis model

As shown in Fig. 1, the DE pendulum consists of a membranous DEG (the yellow area represents the DE and the green areas represent electrodes) with a mass m, which is similar to the spring pendulum. The one end of the DEG is connected to the mass m. The other end is fixed by the fixture which is connected to the frame through the shaft. When the frame is subjected to the external displacement excitation x_f from the mechanical energy sources, the DE pendulum is wiggled around the shaft and the DE membrane can be stretched and contracted, ~~which accomplishes~~ achieving the energy conversion from the mechanical energy to the electrical energy. The parameter θ is the inclined angle of the DE pendulum from its equilibrium position. The DE pendulum length is l_0+l_1, where l_0 is the distance between the top of the DEG and the axial line of the shaft, and l_1 is the length of the DEG.

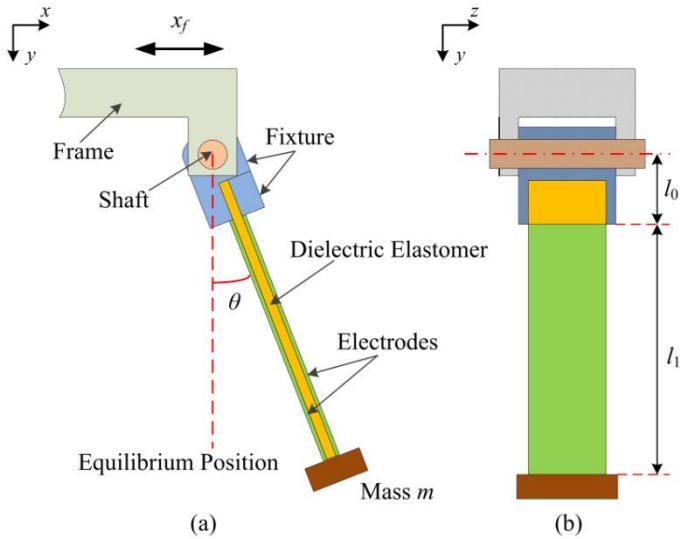

Fig. 1. The sketch of the DE pendulum (a) in the x-y plane and (b) in the y-z plane.

As illustrated in Fig. 2(a), in the un-deformed state, the DE membrane covered

by the electrodes in Fig. 1 is with the initial length L_1, width L_2, and thickness L_3. Under the uniaxial stress s and the voltage Φ, each electrode gets the charge Q, accompanied by a leakage current i_{leak} through the thickness direction, and the membrane is deformed to a homogeneous state, where $l_1=\lambda_1 L_1$, $l_2=\lambda_2 L_2$, $l_3=\lambda_3 L_3$, λ_1, λ_2, and λ_3 are the stretch ratios in the three principal directions, as described in Fig. 2(b). The membrane is considered to be incompressible, therefore, $\lambda_1\lambda_2\lambda_3=1$. In view of the viscoelasticity of the DE materials, a rheological model including two parallel units is utilized [22,33,47], as described in Fig. 2(c). One unit includes a spring α, and the other consists of a spring β with a series-wound dashpot. According to the geometrical relationship, the spring α can deform by the stretch ratios λ_1 and λ_2. For the spring β, the state of the deformation is characterized by the stretch ratios λ_{e1} and λ_{e2}, which are determined by the multiplication rule [22,33,47] as $\lambda_{e1}=\lambda_1/\xi_1$ and $\lambda_{e2}=\lambda_2/\xi_2$, where ξ_1 and ξ_2 are the corresponding inelastic stretch ratios in the dashpot. To describe the strain-stiffening effect of DEs, the Gent model [48] is adopted, and thus, the Helmholtz free energy density function of DEs is expressed as:

$$W_s = -\frac{\mu^\alpha J^\alpha}{2}\log\left(1-\frac{\lambda_1^2+\lambda_2^2+\lambda_1^{-2}\lambda_2^{-2}}{J^\alpha}\right) - \frac{\mu^\beta J^\beta}{2}\log\left(1-\frac{\lambda_1^2\xi_1^{-2}+\lambda_2^2\xi_2^{-2}+\lambda_1^{-2}\lambda_2^{-2}\xi_1^2\xi_2^2}{J^\beta}\right) - \frac{\varepsilon_0\varepsilon_r\Phi^2}{2L_3^2}\lambda_1^2\lambda_2^2, \quad (1)$$

where ε_0 is the vacuum permittivity, ε_r is the dielectric constant of the DE material, μ^α and μ^β are the shear moduli of spring α and spring β, and J^α and J^β are constants of the DE related to the limiting stretch ratios of the two springs.

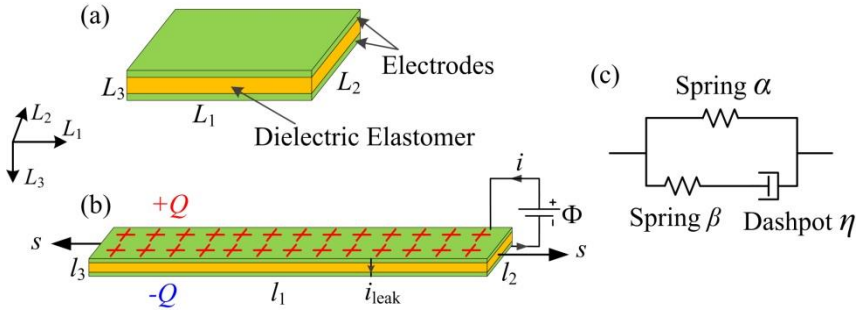

Fig. 2. (a) A DE membrane in the un-deformed state. (b) Subjected to stress s and voltage Φ, the DE membrane is deformed to a charged and stretched state, accompanying with a leakage current i_{leak} through the thickness direction. (c) A rheological model representing the viscoelasticity of the DE membrane with two parallel units.

The dashpot is modeled as a Newtonian fluid, and the deformation rate in the dashpot is described as $\xi_1^{-1}\,\mathrm{d}\,\xi_1/\mathrm{d}\,t$ and $\xi_2^{-1}\,\mathrm{d}\,\xi_2/\mathrm{d}\,t$, which can be expressed as [22,33]

$$\xi_1^{-1}\frac{\mathrm{d}\xi_1}{\mathrm{d}t}=\frac{\mu^{\beta}}{6\eta}\frac{2\lambda_1^2\xi_1^{-2}-\lambda_2^2\xi_2^{-2}-\lambda_1^{-2}\lambda_2^{-2}\xi_1^2\xi_2^2}{1-\left(\lambda_1^2\xi_1^{-2}+\lambda_2^2\xi_2^{-2}+\lambda_1^{-2}\lambda_2^{-2}\xi_1^2\xi_2^2-3\right)\Big/J^{\beta}}, \tag{2}$$

$$\xi_2^{-1}\frac{\mathrm{d}\xi_2}{\mathrm{d}t}=\frac{\mu^{\beta}}{6\eta}\frac{2\lambda_2^2\xi_2^{-2}-\lambda_1^2\xi_1^{-2}-\lambda_1^{-2}\lambda_2^{-2}\xi_1^2\xi_2^2}{1-\left(\lambda_1^2\xi_1^{-2}+\lambda_2^2\xi_2^{-2}+\lambda_1^{-2}\lambda_2^{-2}\xi_1^2\xi_2^2-3\right)\Big/J^{\beta}}, \tag{3}$$

where η is the viscosity of the dashpot. The viscoelastic relaxation time is defined as $t_v=\eta/\mu^{\beta}$.

Fig. 3 shows the EH circuit diagram of the DE pendulum. To describe the leakage current, the DEG is modeled as a parallel-plate capacitor in parallel with a resistor [22], as described in Fig. 3. As the parallel-plate capacitor, the voltage and the charge of the DEG meets $Q=C\Phi$, where $C=\varepsilon_0\varepsilon_r L_1L_2L_3^{-1}\lambda_1^2\lambda_2^2$ represents the capacitance of the DEG. According to the literature [33], the leakage current can be written as

$$i_{leak}=\sigma_{c0}\frac{\Phi L_1L_2\lambda_1^2\lambda_2^2}{L_3}\exp\left(\frac{E}{E_B}\right), \tag{4}$$

where σ_{c0} is the conductivity in a low electric field, $E=\lambda_1\lambda_2\Phi/L_3$ is the electric field, and E_B is an empirical constant. The implementation process of the DE pendulum is summarized as follows. Before the beginning of the EH, the switches S_1 and S_2 are closed, and the capacitor C_p and the DEG are charged by ~~the~~ a power supply until the voltage on the DEG and the capacitor C_p increases to the prescribed initial voltage Φ_{in}. Then, the switches S_1 and S_2 are disconnected, and the external excitation x_f is applied to the frame and the DE pendulum starts to wiggle. During the wiggle of the DE pendulum, the external excitation is converted into the electrical energy and the load resistor R could be powered. At the beginning of the EH, $\Phi=U=\Phi_{\mathrm{in}}$, where U is the voltage across the capacitor C_p. The voltage division circuit is utilized to measure the voltage of the load resistor R through a voltmeter V_1 in parallel with a resistor R_1, as shown in Fig. 3. The resistance ratio $R_1/\mathrm{R}=1/1000$, and thus, the voltage on the load resistor R can be considered to be $U_R=U-\Phi=U_1R/R_1$, where U_1 is the voltage on the divider resistor R_1. In addition, in this paper, the electrodes and the wires are assumed as the perfect conductors. Therefore, the current i through the load resistor R can be expressed as

$$i=\frac{\mathrm{d}\left(C\Phi\right)}{\mathrm{d}t}+i_{leak}=\frac{U_R}{R}=-\frac{\mathrm{d}\left(C_pU\right)}{\mathrm{d}t}. \tag{5}$$

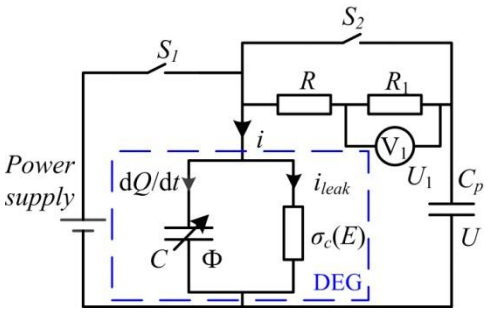

Fig. 3. The EH circuit diagram of the DE pendulum. The EH circuit includes the measuring circuit of the voltage across the load resistor *R*, namely, the voltage division circuit.

The mass of the DEG is much lower than the mass *m* of the DE pendulum, and thus, the kinetic energy and the gravitational potential energy of the DEG are ignored. Thus, the kinetic energy *T* and the potential energy *V* of the DE pendulum are expressed as follows

$$T = \frac{1}{2}m\left(\dot{x}_f + \dot{u}\right)^2 + \frac{1}{2}m\dot{v}^2, \tag{6}$$

$$V = L_1L_2L_3W_s - mg\left(l_0 + L_1\lambda_1\right)\cos\theta, \tag{7}$$

where $u=(l_0+L_1\lambda_1)\sin\theta$, $v=(l_0+L_1\lambda_1)\cos\theta$, $\dot{u} = \mathrm{d}u/\mathrm{d}t$, $\dot{v} = \mathrm{d}v/\mathrm{d}t$, $\dot{x}_f = \mathrm{d}x_f/\mathrm{d}t$, and g is the gravitational acceleration.

The energy dissipation due to the damping can be written as

$$D = \frac{1}{2}c_\theta\left(\left(l_0 + L_1\lambda_1\right)\dot{\theta}\right)^2 + \frac{1}{2}c_l\left(L_1\dot{\lambda}_1\right)^2, \tag{8}$$

where $\dot{\theta} = \mathrm{d}\theta/\mathrm{d}t$, $\dot{\lambda}_1 = \mathrm{d}\lambda_1/\mathrm{d}t$, c_θ is the damping in the circumferential direction, and c_l is the damping in the radial direction.

Lagrange' equation is utilized to build the motion equations of the DE pendulum, which is expressed as follows.

$$\frac{d}{dt}\left(\frac{\partial\left(T-V\right)}{\partial\dot{q}_i}\right) - \frac{\partial\left(T-V\right)}{\partial q_i} + \frac{\partial D}{\partial\dot{q}_i} = 0, \tag{9}$$

where q_i (i=1,2,3) denotes the variables θ, λ_1, and λ_2.

Substituting equations (1) and (6)-(8) into equation (9), motion equations of the DE pendulum can be obtained as follows.

$$\begin{aligned} &m\left(L_1\lambda_1 + l_0\right)^2\ddot{\theta} + c_\theta\left(L_1\lambda_1 + l_0\right)^2\dot{\theta} + 2mL_1\left(L_1\lambda_1 + l_0\right)\dot{\lambda}_1\dot{\theta} \\ &+mg\left(L_1\lambda_1 + l_0\right)\sin\theta + m\ddot{x}_f\left(L_1\lambda_1 + l_0\right)\cos\theta = 0 \end{aligned}, \tag{10}$$

$$\frac{mL_1}{L_2L_3}\ddot{\lambda}_1+\frac{c_lL_1}{L_2L_3}\dot{\lambda}_1-\frac{m\left(l_0+L_1\lambda_1\right)}{L_2L_3}\dot{\theta}^2+\frac{\mu^{\alpha}\left(\lambda_1-\lambda_1^{-3}\lambda_2^{-2}\right)}{1-\left(\lambda_1^2+\lambda_2^2+\lambda_1^{-2}\lambda_2^{-2}-3\right)\Big/J^{\alpha}}$$
$$-\frac{\mu^{\beta}\left(\lambda_1\xi_1^{-2}-\lambda_1^{-3}\lambda_2^{-2}\xi_1^2\xi_2^2\right)}{1-\left(\lambda_1^2\xi_1^{-2}+\lambda_2^2\xi_2^{-2}+\lambda_1^{-2}\lambda_2^{-2}\xi_1^2\xi_2^2-3\right)\Big/J^{\beta}}-\frac{\varepsilon_0\varepsilon_r\Phi^2}{L_3^2}\lambda_1\lambda_2^2 \quad , \tag{11}$$
$$-\frac{mg}{L_2L_3}\cos\theta+\frac{m\ddot{x}_f}{L_2L_3}\sin\theta=0$$

$$-\frac{\varepsilon_0\varepsilon_r\Phi^2}{L_3^2}\lambda_2\lambda_1^2+\frac{\mu^{\alpha}\left(\lambda_2-\lambda_2^{-3}\lambda_1^{-2}\right)}{1-\left(\lambda_1^2+\lambda_2^2+\lambda_1^{-2}\lambda_2^{-2}-3\right)\Big/J^{\alpha}}$$
$$-\frac{\mu^{\beta}\left(\lambda_2\xi_2^{-2}-\lambda_2^{-3}\lambda_1^{-2}\xi_1^2\xi_2^2\right)}{1-\left(\lambda_1^2\xi_1^{-2}+\lambda_2^2\xi_2^{-2}+\lambda_1^{-2}\lambda_2^{-2}\xi_1^2\xi_2^2-3\right)\Big/J^{\beta}}=0 \quad , \tag{12}$$

where $\ddot{\lambda}_1=\mathrm{d}^2\lambda_1/\mathrm{d}t^2$, $\ddot{\theta}=\mathrm{d}^2\theta/\mathrm{d}t^2$, and $\ddot{x}_f=\mathrm{d}^2x_f/\mathrm{d}t^2$.

In equations (10) and (11), the external excitation $\ddot{x}_f$ is the random process, which is governed by the following equation [49,50]

$$\ddot{x}_f(t)=A\cos\left(\omega_n t+\sigma W(t)\right), \tag{13}$$

where A is the excitation amplitude, ω_n is the circular frequency, $W(t)$ is a standard Wiener process, and σ is the intensity of the white noise $\zeta(t)=\mathrm{d}W(t)/\mathrm{d}t$. The circular frequency can be expressed as $\omega_n=2\pi f_n$, where f_n is the excitation frequency. The power spectrum density of the random process $\ddot{x}_f$ is [49]

$$S_{\ddot{x}_f}(\omega)=\frac{A^2\sigma^2}{2}\frac{\omega_n^2+\omega^2+\sigma^4/4}{\left(\omega_n^2-\omega^2+\sigma^4/4\right)^2+\omega^2\sigma^4}, \tag{14}$$

When $A=\sigma/\sqrt{2}\to\infty$, the power spectrum density $S_{\ddot{x}_f}(\omega)$ becomes the uniformly distributed power spectrum of white noise. When $\sigma\to 0$, the power spectrum density $S_{\ddot{x}_f}(\omega)$ is vanishing over the entire frequency range except at $\omega=\pm\omega_n$ where $S_{\ddot{x}_f}(\omega)$ goes to the infinity, which is ~~the~~ a typical spectrum of the random narrow-band noise. In this paper, the EH performance of the DE pendulum under the random narrow-band excitation is studied.

In this paper $\zeta(t)$ is selected as Gaussian white noise with zero mean, which has a constant power spectrum density and is physically unrealized. Therefore, for the numerical simulation, the power spectrum density of $\zeta(t)$ is taken as

$$S_{\zeta}(\omega)=\begin{cases}S_0, & 0<\omega\le 2\omega_0\\ 0, & \omega>2\omega_0\end{cases}, \tag{15}$$

where $2\omega_0=4\pi f_0$ is the upper frequency limit of the power spectrum.

In this paper, the average power density and the effective voltage are used to evaluate the EH performance of the DE pendulum. The average power density and the effective voltage from t_1 to t_2 can be expressed as follows

$$P=\frac{1}{(t_2-t_1)L_1L_2L_3}\int_{t_1}^{t_2}\frac{U_R^2}{R}\mathrm{d}t, \tag{16}$$

$$U_e=\sqrt{L_1L_2L_3PR}, \tag{17}$$

In this paper, by utilizing the fourth-order Runge–Kutta algorithm to solve a set of differential-algebraic equations, i.e., equations (2)-(5) and (10)-(13), the time evolution of parameters θ, λ_1, λ_2, ξ_1, ξ_2, Φ, U, U_R, Q, and i_{leak} can be obtained. Before the differential-algebraic equations are solved, the external excitation and the initial conditions need to be given.

(用了太多的 in this paper)

3. Experimental Verification

In order to further verify the operating principle of the DE pendulum, the voltage on the load resistor R is measured by the voltage division circuit mentioned above. Polyacrylate VHB elastomer (3M Company) is used as the DE material because of its high energy density and large deformability. Carbon grease (CG846-80G, MG Chemicals) is chosen as the compliant electrode material. Carbon grease is smeared on both surfaces of VHB elastomer~~, which~~ to forms a membranous DEG. A prototype of the DE pendulum is shown in Fig. 4. Fig. 5 illustrates the experimental procedure of the DE pendulum. The high-voltage power supply (Model 610E, Trek) is used to provide the initial voltage of the DEG and the capacitor C_p. The servomotor (Model AKM54L Kollmorgen) is used to generate the external excitation applied to the DE pendulum. The experimental data of the voltage on the load resistor R can be collected by a DAQ card (Model USB-6218, National Instruments), and inputted into the computer to obtain the results. In the analysis, the parameters of the DE pendulum and the external excitation are selected as L_1=25mm, L_2=27 mm, L_3=0.5 mm, l_0=45 mm, $\varepsilon_0=8.85\times10^{-12}$ F/m, μ^{α}=15 kPa, μ^{β}=50 kPa, J^{α}=110, J^{β}=55, ε=3.5, E_B=40 MV/m, $\sigma_{c0}=3.23\times10^{-14}$ S/m, C_p=1 μF, $c_\theta=c_l$=0.35 N/(m/s), R=500 MΩ, g=9.8 m/s^2, t_v=1 s, f_n=1.57 Hz, m=0.128 kg, A=3.89 m/s^2, σ=0, S_0=1, f_0=2.5 Hz [6,22,33,35,36].

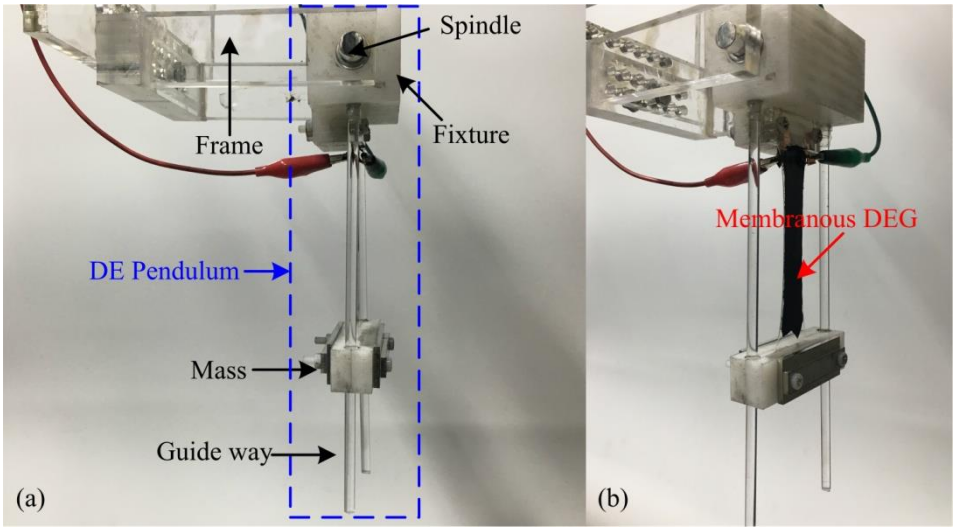

Fig. 4. The prototype of the DE pendulum.

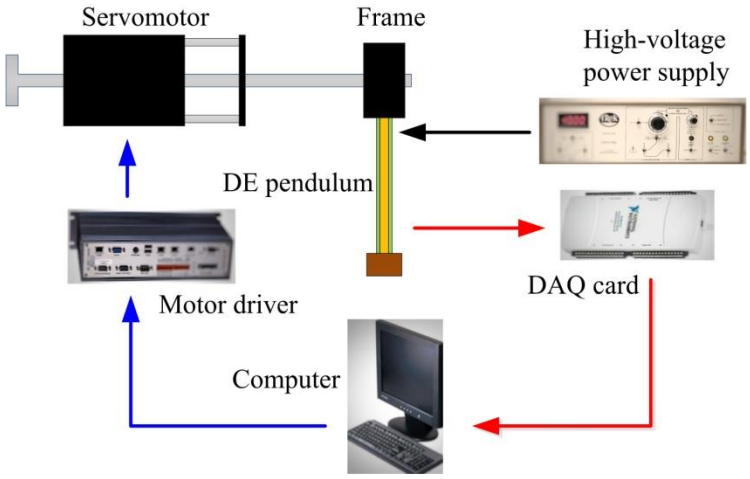

Fig. 5. The experimental procedure of the DE pendulum.

Fig. 6 shows the voltage U_R on the load resistor R under Φ_{in}=1500 V and Φ_{in}=2000 V. In this analysis, the initial conditions are listed as follows. When Φ_{in}=1500 V, $\lambda_1(0)$=5.003, $\lambda_2(0)$=0.502, $\theta(0)$=0, $\dot{\lambda}_1(0)=0$, $\dot{\lambda}_2(0)=0$, and $\dot{\theta}(0)=0$, and when Φ_{in}=2000 V, $\lambda_1(0)$=5.013, $\lambda_2(0)$=0.585, $\theta(0)$=0, $\dot{\lambda}_1(0)=0$, $\dot{\lambda}_2(0)=0$, and $\dot{\theta}(0)=0$. In addition, the simulation results and the experimental results are displayed from 10 s to 20 s. It can be noticed from Fig. 6 that the simulation results are consistent with the experimental results, indicating the feasibility of the operating principle of the DE pendulum and the predictability of the developed dynamic model. In addition, the slight fluctuation in the amplitude of the voltage across the load resistor R in the experiments is mainly due to the friction of the guide way and the friction of the spindle.

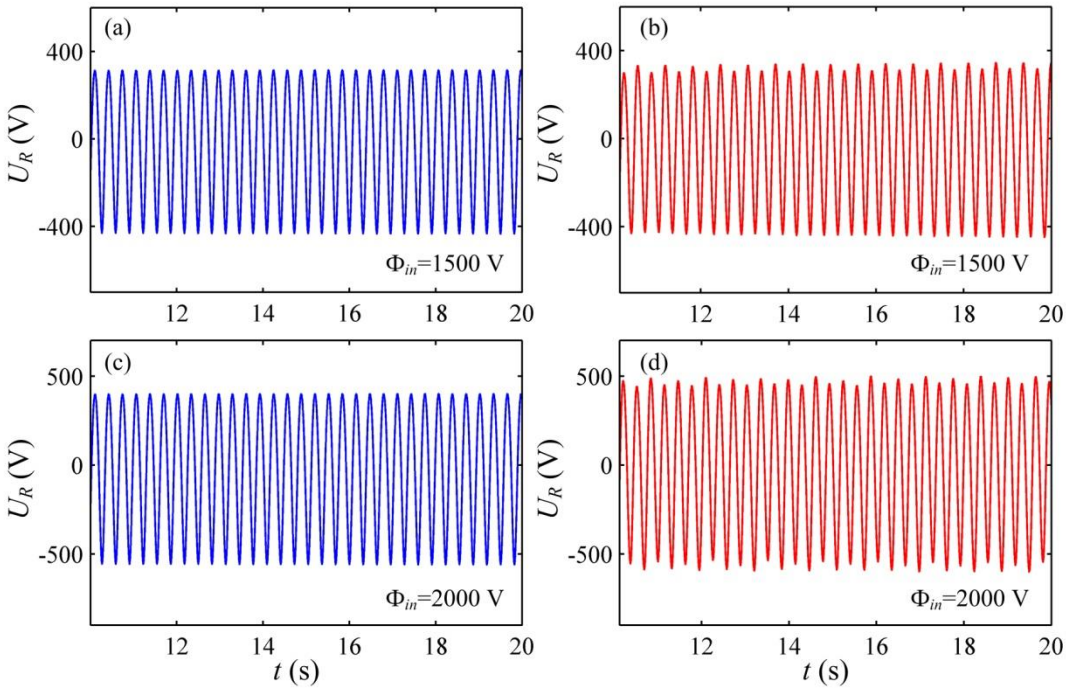

Fig. 6. The voltage U_R on the load resistor R under Φ_{in}=1500 V and Φ_{in}=2000 V. (a) and (c) the simulation results, and (b) and (d) the experimental results.

4. Dynamic behavior

In this section, the dynamic behavior of the DE pendulum under the random excitation is investigated by employing phase diagrams, Poincaré maps, and bifurcation diagrams. If all the points in Poincaré maps overlap to one point or several points, the DE pendulum can undergo a periodic motion. When all the points in Poincaré maps form a closed cycle, the DE pendulum can experience the quasi-periodic motion. If all the points in Poincaré maps are disordered, an aperiodic motion of the DE pendulum is achieved. The system parameters of the DE pendulum remain unchanged as L_1=25mm, L_2=27 mm, L_3=0.5 mm, l_0=45 mm, ε_0=8.85×10^{-12} F/m, μ^{α}=15 kPa, μ^{β}=50 kPa, J^{α}=110, J^{β}=55, ε=3.5, E_B=40 MV/m, σ_{c0}=3.23×10^{-14} S/m, C_p=1 μF, c_θ=c_l=0.35 N/(m/s), R=200 MΩ, g=9.8 m/s^2, t_v=1 s, m=0.128 kg, Φ_{in}=1100 V [6,22,33,35,36]. The parameters of the random excitation are f_n=1.25 Hz, A=2.47 m/s^2, σ=0.02, S_0=1, f_0=2.5 Hz. The time from 20 s to 120 s is selected to exhibit phase diagrams, Poincaré maps, and bifurcation diagrams. In this simulation, the initial conditions are $\lambda_1(0)$=5, $\lambda_2(0)$=0.473, $\theta(0)$=0, $\dot{\lambda}_1(0)=0$, $\dot{\lambda}_2(0)=0$, and $\dot{\theta}(0)=0$. We vary the values of the parameters σ, S_0, and f_0 to analyze the effect of the random excitation on the dynamic behavior of the DE pendulum.

The dynamic response of the DE pendulum for different values of the intensity σ of Gaussian white noise is plotted in Fig. 7. Fig. 7(a) shows the variation of the stretch

ratio λ_1 with the time at the intensity σ=0. It can be seen from Fig. 7(a) that the curve of the stretch ratio λ_1 looks like a harmonic wave and the amplitude of the stretch ratio λ_1 remains constant. The reason for this is that when the intensity σ=0, the external excitation is transferred from the random excitation to the harmonic excitation. Fig. 7(b) describes the phase diagram of the stretch ratio λ_1 at the intensity σ=0. It can be noticed from Fig. 7(b) that the phase trajectory of the stretch ratio λ_1 exhibits a single closed cycle, which indicates the DE pendulum is in a stable state. Fig. 7(c) depicts Poincaré map of the stretch ratio λ_1 at the intensity σ=0. As can be seen, Poincaré map overlaps to one point, which demonstrates the periodic motion of the DE pendulum. When the intensity σ increases to 0.02, the external excitation becomes the random excitation. The harmonic wave of the stretch ratio λ_1 could vanish and the amplitude of the stretch ratio λ_1 could slightly fluctuate, as shown in Fig. 7(d). It can be observed from Fig. 7(e) that the phase trajectory of the stretch ratio λ_1 becomes a diffused limit cycle, which shows a complicated nonlinear vibration behavior. Poincaré map in Fig. 7(f) is disordered and does not form a closed cycle, which reveals that the periodic motion of the DE pendulum vanishes. When the intensity σ further increases, such as σ=0.04 and σ=0.06, the variation of the stretch ratio λ_1 could still exhibit the anharmonic behavior (see Fig. 7(g) and (j)). It can also be seen from Fig. 7(g) and (j) that the amplitude of the stretch ratio λ_1 decreases and its fluctuation can become significant. From Fig. 7(h) and (k), we can notice that the phase trajectory of the stretch ratio λ_1 becomes the more diffused limit cycle and the width of the diffused limit cycle can enlarge, which infers a more complicated nonlinear vibration of the DE pendulum. From Fig. 7(i) and (l), it can be seen that the points in Poincaré maps are still disordered, indicating that the DE pendulum experiences the aperiodic vibration. In addition, when the intensity σ increases, the maximum stretch ratio λ_{max} can decrease and the minimum stretch ratio λ_{min} can increase, namely, the change of the stretch ratio λ_1 in a harvesting cycle can decrease, which can affect the EH performance of the DE pendulum due to decreasing the capacitance change of the DE membrane. Fig. 8 shows the bifurcation diagram of the stretch ratio λ_1 with the intensity σ of Gaussian white noise. It can be seen from Fig. 8 that with the increase in the intensity σ, the change of the stretch ratio λ_1 in a harvesting cycle can decrease.

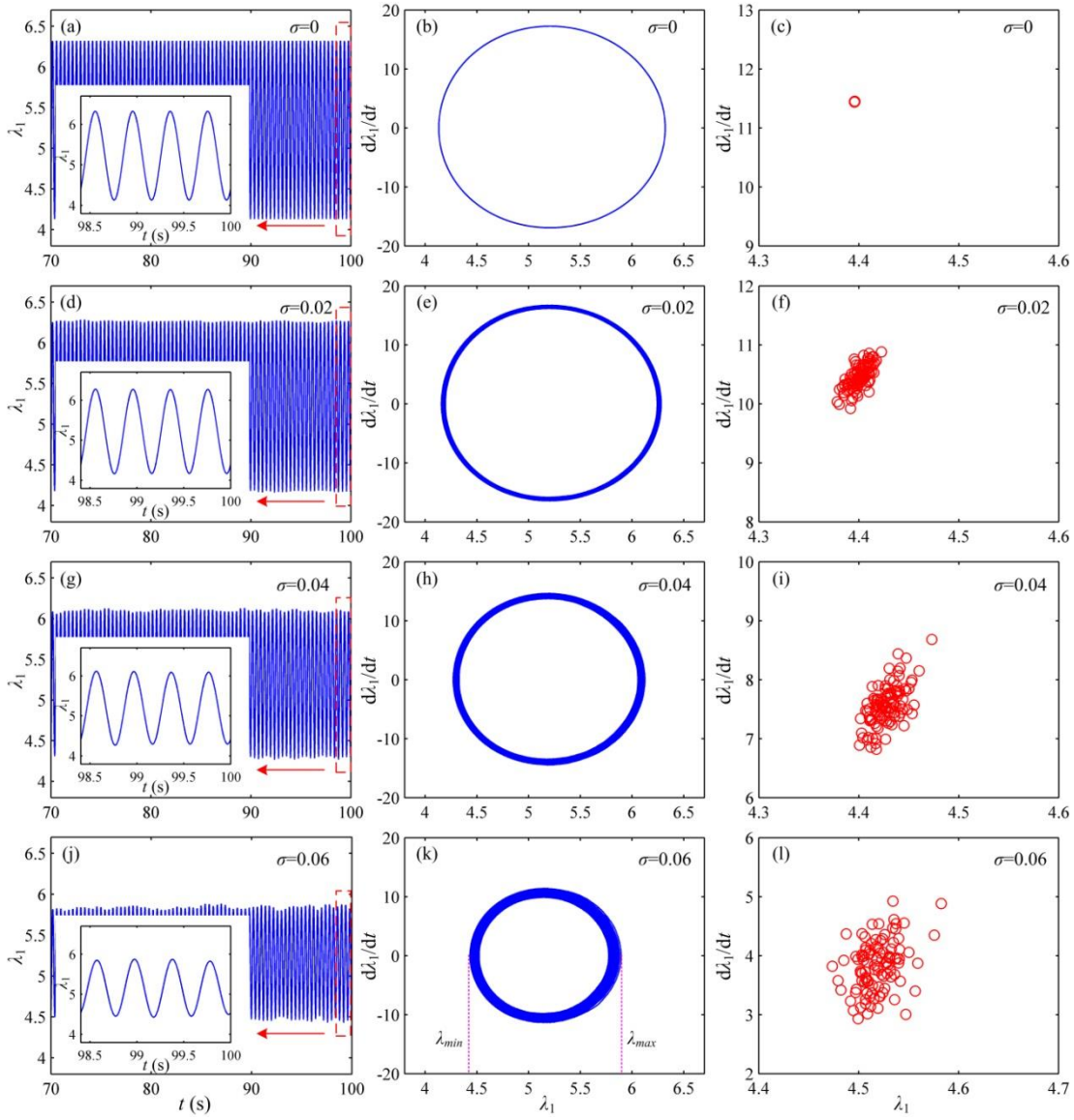

Fig. 7. Dynamic behavior of the DE pendulum under the random excitation for different values of the intensity σ. (a), (d), (g), and (j) the stretch ratio λ_1 of the DE membrane, (b), (e), (h), and (k) the phase diagram of the stretch ratio λ_1, and (c), (f), (i), and (l) Poincaré map of the stretch ratio λ_1.

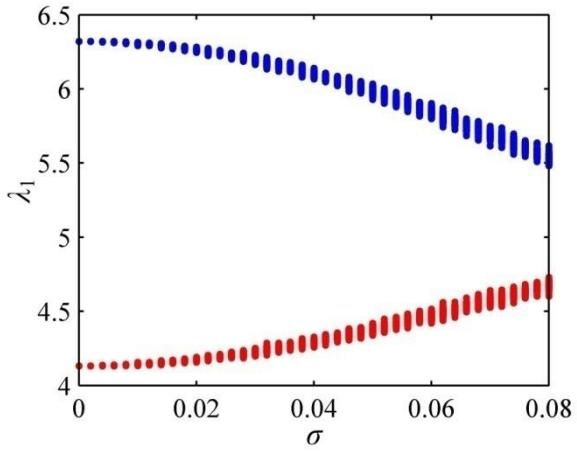

Fig. 8. Bifurcation diagram of the stretch ratio λ_1 with the intensity σ as a control parameter.

Fig. 9 shows the dynamic response of the DE pendulum under the random excitation for different values of the power spectrum density S_0 of Gaussian white noise. Similar to the situation of σ=0, it can be noticed from Fig. 9(a) that at S_0=0, the DE pendulum is in a stable state and the variation of the stretch ratio λ_1 with the time is periodic. This can be explained as follows. When S_0=0, Gaussian white noise can vanish, and thus, the external excitation becomes the harmonic excitation. A single closed phase trajectory is described in Fig. 9(b), indicating that the motion of the DE pendulum is periodic, which is also verified by the one coincident point in Poincaré map of Fig. 9(c). When the power spectrum density S_0 increases to 2, the slight fluctuation can be generated for the amplitude of the stretch ratio λ_1 due to the effect of Gaussian white noise (see Fig. 9(d)). It can be seen from Fig. 9(e) that the phase trajectory of the stretch ratio λ_1 can become a diffused limit cycle, indicating that the nonlinearity of the vibration of the DE pendulum is enhanced. From Fig. 9(f), we can notice that the points in Poincaré map are disordered, which can infers that the motion of the DE pendulum loses the periodicity and exhibits the aperiodic behavior. When the power spectrum density S_0 further increases, such as S_0=4 and S_0=6, the amplitude of the stretch ratio λ_1 can decrease and its fluctuation can strengthen (see Fig. 9(g) and (j)). It can be seen from Fig. 9(h) and (k) that the phase trajectory of the stretch ratio λ_1 shows a diffused limit cycle with the large cycle width, corresponding to the more disordered points in Poincaré maps of Fig. 9(i) and (l), which indicates that the nonlinear aperiodic motion of the DE pendulum becomes more complex. It can be also seen from Fig. 9 that as the power spectrum density S_0 increases, the maximum stretch ratio λ_{max} decreases and the minimum stretch ratio λ_{min} increases, resulting in reducing the change of the stretch ratio λ_1 of the DE membrane in a harvesting cycle.

This will have an effect on the EH performance of the DE pendulum ~~due to that~~ since the capacitance change of the DE membrane in a harvesting cycle is altered. Fig. 10 shows the bifurcation diagram of the stretch ratio λ_1 with the power spectrum density S_0 of Gaussian white noise. It can also be demonstrated from Fig. 10 that with the increase in the power spectrum density S_0, the change of the stretch ratio λ_1 of the DE membrane in a harvesting cycle can decrease.

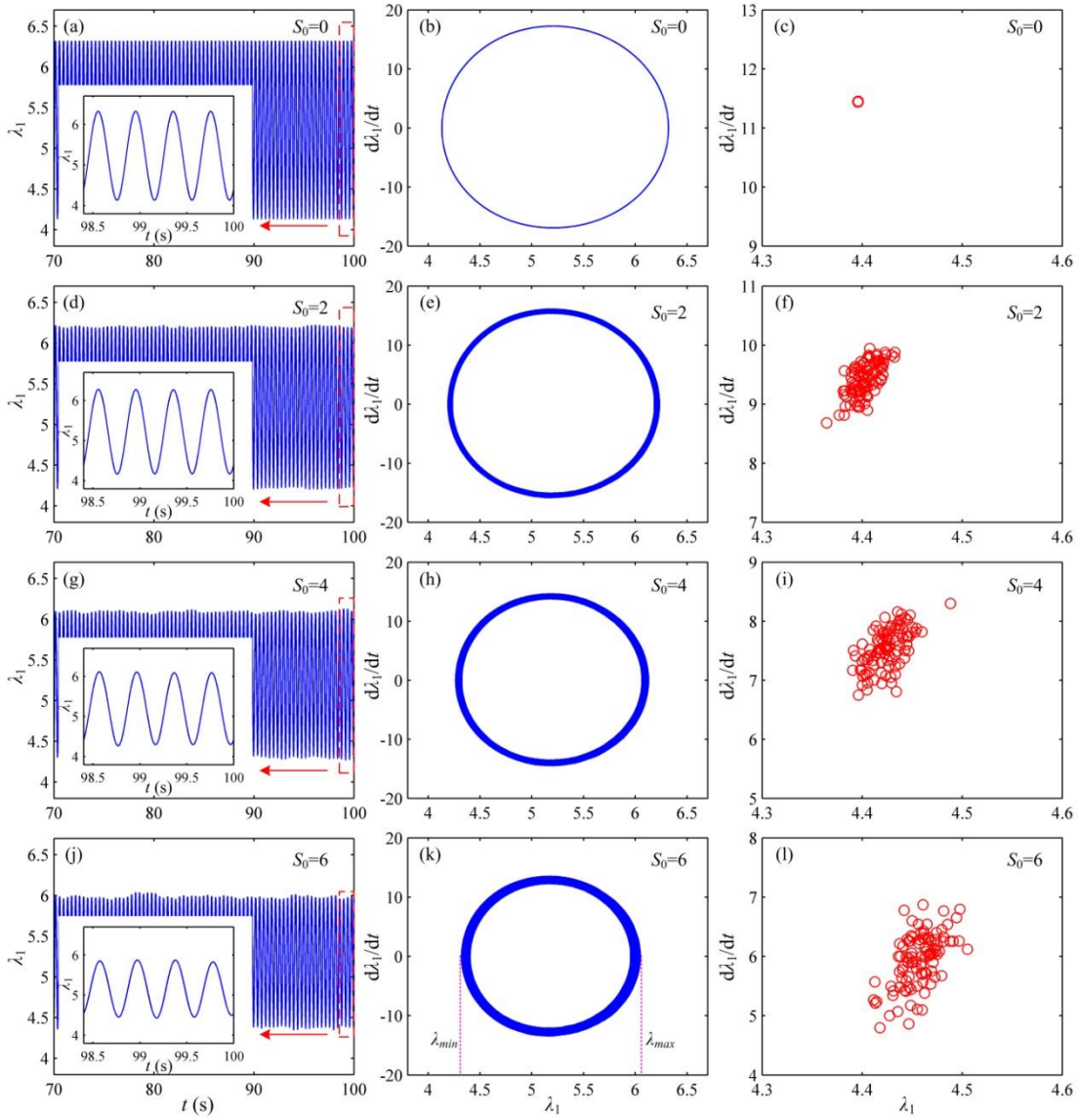

Fig. 9. Dynamic behavior of the DE pendulum under the random excitation for different values of the power spectrum density S_0. (a), (d), (g), and (j) the stretch ratio λ_1 of the DE membrane, (b), (e), (h), and (k) the phase diagram of the stretch ratio λ_1, and (c), (f), (i), and (l) Poincaré map of the stretch ratio λ_1.

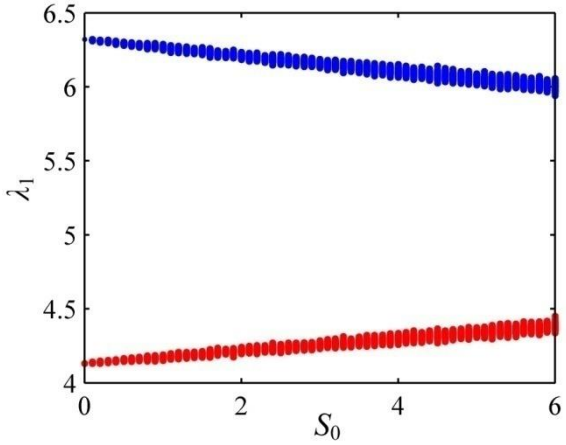

Fig. 10. Bifurcation diagram of the stretch ratio λ_1 with the power spectrum density S_0 as a control parameter.

Dynamic response of the DE pendulum under the random excitation for different values of the upper limiting frequency f_0 of Gaussian white noise is plotted in Fig. 11. It can be seen that the DE pendulum is in ~~the~~ an unstable state and the amplitude of the stretch ratio λ_1 can fluctuate (see Fig. 11(a), (d), (g), and (j)). It can also be seen that with the increase in the upper limiting frequency f_0, the fluctuation of the amplitude of the stretch ratio λ_1 can weaken. The phase trajectory of the stretch ratio λ_1 presents a diffused limit cycle (see Fig. 11(b), (e), (h), and (k)) and Poincaré maps are disordered (see Fig. 11(c), (f), (i), and (l)), which indicates that the DE pendulum undergoes the aperiodic motion. Moreover, with the increase in the upper limiting frequency f_0, the width of the diffused limit cycle can decrease and the disorder of the points in Poincaré maps can weaken, and thus, it can be inferred that decreasing the upper limiting frequency f_0 can result in the more complicated nonlinear aperiodic motion of the DE pendulum. Furthermore, from Fig. 11, we can also notice that as the upper limiting frequency f_0 increases, the maximum stretch ratio λ_{max} can increase and the minimum stretch ratio λ_{min} can decrease, and thus, the change of the stretch ratio λ_1 of the DE membrane in a harvesting cycle can increase, which contributes to enhancing the EH performance of the DE pendulum due to enlarging the capacitance change of the DE membrane in a harvesting cycle. Fig. 12 describes the bifurcation diagram of the stretch ratio λ_1 with the upper limiting frequency f_0 of Gaussian white noise. It can also be noticed from Fig. 12 that with the increase in the upper limiting frequency f_0, the maximum stretch ratio λ_{max} can first increase and then trend to the saturation, while the minimum stretch ratio λ_{min} can first decrease and then trend to the saturation. Thus, as the upper limiting frequency f_0 enlarges, the change of the stretch ratio λ_1 of the DE membrane in a harvesting cycle can first increase and then

trend gradually to the saturation.

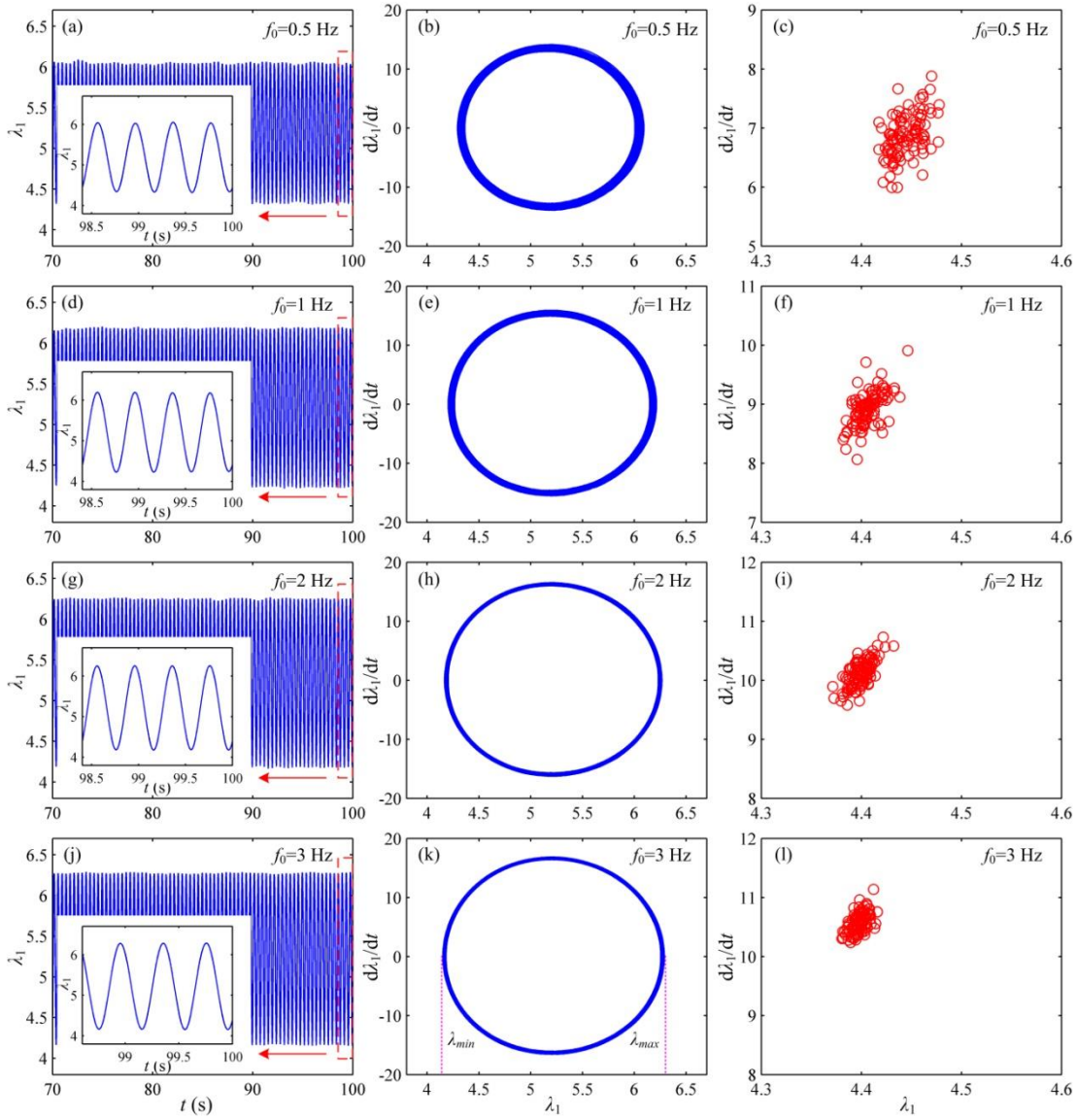

Fig. 11. Dynamic behavior of the DE pendulum under the random excitation for different values of the upper limiting frequency f_0. (a), (d), (g), and (j) the stretch ratio λ_1 of the DE membrane, (b), (e), (h), and (k) the phase diagram of the stretch ratio λ_1, and (c), (f), (i), and (l) Poincaré map of the stretch ratio λ_1.

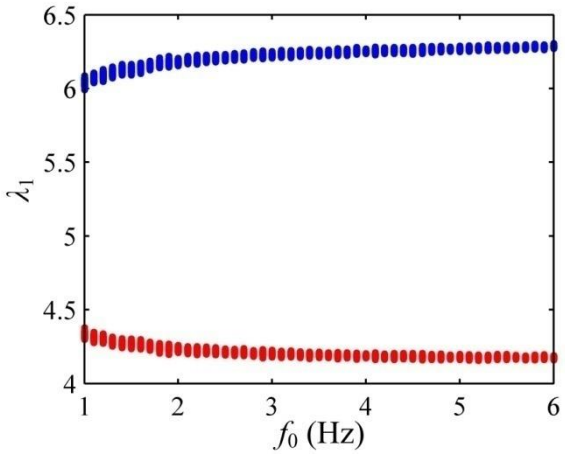

Fig. 12. Bifurcation diagram of the stretch ratio λ_1 with the upper limiting frequency f_0 as a control parameter.

5. Energy harvesting performance

In this section, the EH performance of the DE pendulum under the random excitation is investigated. The average power density and the effective voltage are used as the performance parameters to evaluate the EH performance of the DE pendulum. The system parameters of the DE pendulum are selected as L_1=25mm, L_2=27 mm, L_3=0.5 mm, l_0=45 mm, ε_0=8.85×10^{-12} F/m, μ^{α}=15 kPa, μ^{β}=50 kPa, J^{α}=110, J^{β}=55, ε=3.5, E_B=40 MV/m, σ_{c0}=3.23×10^{-14} S/m, C_p=1 μF, c_θ=c_l=0.35 N/(m/s), R=200 MΩ, g=9.8 m/s^2, t_v=1 s, m=0.128 kg, Φ_{in}=1100 V [6,22,33,35,36]. The related parameters of the random excitation are f_n=1.57 Hz, A=3.89 m/s^2, σ=0.02, S_0=1, f_0=2.5 Hz. The time from 20 s to 120 s is selected to calculate the average power density and the effective voltage. By varying the values of the parameters σ, S_0, and f_0, the effect of the random excitation on the EH performance of the DE pendulum is analyzed.

Fig. 13 shows the effect of the intensity σ of Gaussian white noise on the EH performance of the DE pendulum for different values of the mass m. In this simulation, the initial conditions are $\lambda_1(0)$=5.5 and $\lambda_2(0)$=0.455 at m=0.151 kg, $\lambda_1(0)$=5 and $\lambda_2(0)$=0.473 at m=0.128 kg, $\lambda_1(0)$=4.5 and $\lambda_2(0)$=0.494 at m=0.109 kg, and $\lambda_1(0)$=4 and $\lambda_2(0)$=0.519 at m=0.093 kg. The other initial conditions are $\theta(0)$=0, $\dot{\lambda}_1(0)=0$, $\dot{\lambda}_2(0)=0$, and $\dot{\theta}(0)=0$. It can be seen from Fig. 13(a) that as the intensity σ increases, the average power density P can decrease. The reason for this can be explained as follows. It ~~can be~~ is known that the larger the capacitance change of the DEG in a harvesting cycle is, the more the harvested electrical energy is. As mentioned above, with the increase in the intensity σ, the change of the stretch ratio of the DE membrane in a harvesting cycle can decrease, and thus, the capacitance

change of the DEG in a harvesting cycle can reduce. Therefore, at the small intensity σ, the high average power density can be achieved. In addition, the trend of the average power density P with the intensity σ could not be affected by the mass m. It can also be noticed from Fig. 13(a) that with the increase in the mass m, the average power density P can decrease. The reason for this can be explained as follows. The natural frequency of the DE pendulum is $f_p = \sqrt{g/\left(l_0 + L_1\lambda_{pre}\right)}/\left(2\pi\right)$, where λ_{pre} is the stretch ratio of the DE membrane along the direction of L_1 when the DE pendulum is in static state. According to the given initial conditions, it can be inferred that $\lambda_{pre}=\lambda_1(0)$. When the excitation frequency f_n is close to the nature frequency f_p of the DE pendulum, the high average power density can be achieved. As the mass m decreases, the stretch ratio $\lambda_1(0)$ in the initial condition can decrease, and thus, the natural frequency f_p of the DE pendulum can increase. At m=0.093 kg, the nature frequency f_p of the DE pendulum reaches the maximum value and f_p=1.28 Hz, which is still lower than the excitation frequency f_n=1.57 Hz. This indicates that the smaller the mass m is, the closer the excitation frequency f_n is to the nature frequency f_p of the DE pendulum, and thus, enlarging the mass m can decrease the average power density. According to equation (17), for the given parameters L_1, L_2, L_3, and R, the variation trend of the average power density P is in agreement with that of the effective voltage U_e. Therefore, as the mass m or the intensity σ increases, the effective voltage U_e can reduce (see Fig. 13(b)).

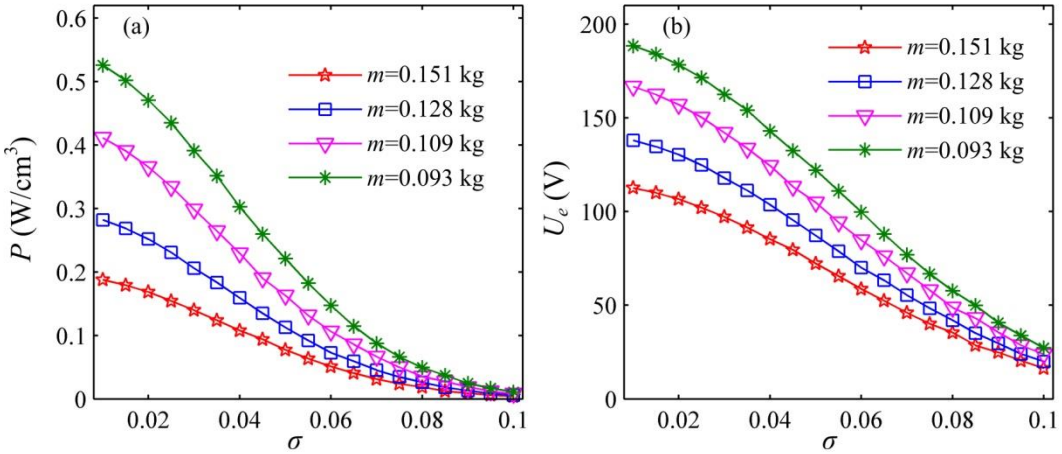

Fig. 13. The effect of the intensity σ of Gaussian white noise on the EH performance of the DE pendulum for different values of the mass m. (a) The average power density and (b) the effective voltage.

As described in Fig. 14, the effect of the power spectrum density S_0 of Gaussian white noise on the EH performance of the DE pendulum for different values of the load

resistance R is analyzed. In this simulation, the initial conditions are $\lambda_1(0)=5$, $\lambda_2(0)=0.473$, $\theta(0)=0$, $\dot{\lambda}_1(0)=0$, $\dot{\lambda}_2(0)=0$, and $\dot{\theta}(0)=0$. As can be seen from Fig. 14 (a), with the increase in the power spectrum density S_0, the average power density P can decrease. The explanation for this is as follows. As mentioned above, as the power spectrum density S_0 increases, the change of the stretch ratio of the DEG in a harvesting cycle can decrease, and thus, the capacitance change of the DEG in a harvesting cycle can decrease, which causes the harvested electrical energy to reduce. Similarly, as the power spectrum density S_0 increases, the effective voltage U_e can decrease (see Fig. 14(b)). The reason for this is that according to equation (17), there is a positive correlation between the average power density P and the square of the effective voltage U_e when the parameters L_1, L_2, L_3, and R are given. It can also be seen from Fig. 14 (a) that with the increase in the load resistance R, the average power density P can first increase and then decrease. This can be explained as follows. The DEG can be regarded as a power supply with the internal resistance (the internal resistance is the capacitive reactance of the DEG). It can be known that the maximum electrical power is achieved when the load resistance is equal to the internal resistance. Thus, the variation of the average power density P with the load resistance R exhibits the non-monotonic behavior. As shown in Fig. 14(b), as the load resistance R increases, the effective voltage U_e can increase. The reason for this can be explained as follows. The larger the load resistance R is, the lower the charge transfer between the DEG and the capacitor C_p is, and thus, the larger the amplitude of the voltage on the load resistance R is, resulting in higher effective voltage U_e.

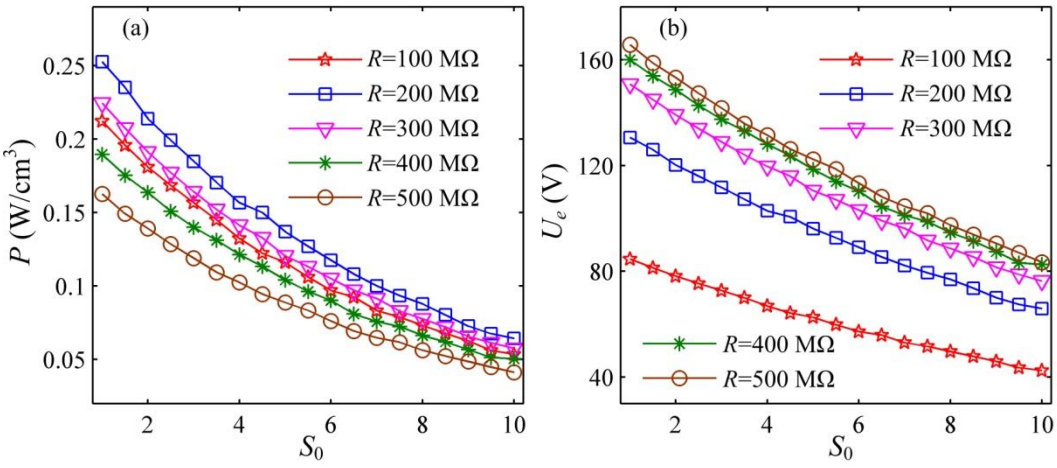

Fig. 14. The effect of the power spectrum density S_0 of Gaussian white noise on the EH performance of the DE pendulum for different values of the load resistance R. (a) The average power density and (b) the effective voltage.

Fig. 15 depicts the effect of the upper limiting frequency f_0 of Gaussian white noise on the EH performance of the DE pendulum for different values of the initial length L_1 of the DEG. In this calculation, the initial conditions are $\lambda_1(0)=5$, $\lambda_2(0)=0.473$, $\theta(0)=0$, $\dot{\lambda}_1(0)=0$, $\dot{\lambda}_2(0)=0$, and $\dot{\theta}(0)=0$. It can be seen from Fig. 15 that with the increase in the upper limiting frequency f_0, both the average power density P and the effective voltage U_e can first increase rapidly and then trends to the saturation. This is due to that as the upper limiting frequency f_0 increases, the change of the stretch ratio of the DEG can first increase and then trends to the saturation. From equation (17), the effective voltage U_e can increase with the increase in the average power density P for the given parameters L_1, L_2, L_3, and R. Thus, increasing the upper limiting frequency f_0 can improve the effective voltage U_e. In addition, it can also be from Fig. 15 that increasing the initial length L_1 can reduce both the average power density P and the effective voltage U_e. The reason can be explained as follows. As the initial length L_1 of the DEG, the natural frequency f_p of the DE pendulum can decrease, which is far from the excitation frequency f_n. Thus, with the increase in the initial length L_1 of the DEG, the average power density P can decrease.

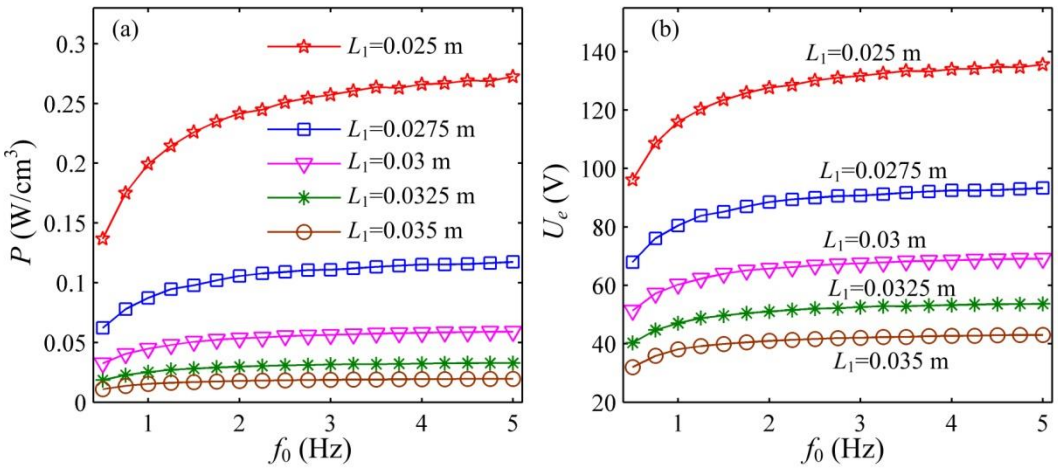

Fig. 15. The effect of the upper limiting frequency f_0 of Gaussian white noise on the EH performance of the DE pendulum for different values of the initial length L_1 of the DEG. (a) The average power density and (b) the effective voltage.

The above simulation results can be used to design the DE pendulum for its best performance, based on a given set of the vibration environmental constraints. For example, the parameters of the random excitation that is converted into the electrical energy are assumed as f_n=1.57 Hz, σ=0.02, S_0=1, and f_0=2.5 Hz. When some parameters of the DE pendulum are limited, such as L_2=27 mm, L_3=0.5 mm, and m=0.0128 kg, the highest average power density will be achieved by optimizing the

load resistance R and the length L_1 of the DE membrane. According to the simulation results, it can be known that decreasing the length L_1 can improve the average power density. Due to the monotonic decreasing trend, the minimum value of the length L_1, namely, L_1=25 mm, should be selected. After the length L_1 is selected, the load resistance R is further optimized. From the above simulations, the variation of the average power density with the load resistance R is non-monotonic. At R=200 MΩ, the average power density reaches the maximum value. In view of this, the load resistance R=200 MΩ should be chosen. Therefore, the DE pendulum generates the highest average power density at R=200 MΩ and L_1=25 mm. If the highest effective voltage is the design goal, the DE pendulum is designed as follows. As mentioned above, with the increase in the length L_1, the effective voltage can decrease, and thus, the length L_1=25 mm should be selected. On this basis, the load resistance R is further adjusted. From the results achieved in this paper, it can be known that increasing the load resistance R can improve the effective voltage. Due to the monotonic increasing trend, the load resistance R=500 MΩ should be chosen. Therefore, the highest effective voltage is obtained at R=500 MΩ and L_1=25 mm.

6. Conclusions

This paper investigates the EH performance of the DE pendulum under the random excitation. The DE pendulum that is similar to the spring pendulum consists of a DE membrane with a mass, which can convert the vibration energy into the electrical energy. The dynamic analysis model of the DE pendulum under the random excitation is developed~~, which is~~ and verified by the experimental results. On this basis, the random dynamic response of the DE pendulum is analyzed. The random excitation is $\ddot{x}_f(t) = A\cos\left(\omega_n t + \sigma W(t)\right)$, where $W(t)$ is a standard Wiener process and σ is the intensity of Gaussian white noise $\zeta(t)=\mathrm{d}W(t)/\mathrm{d}t$. The effect of the random excitation is executed by varying the intensity, the power spectrum density, and the upper limiting frequency of Gaussian white noise. The phase trajectory and Poincaré map of the stretch ratio of the DE membrane in the length direction reveal that the DE pendulum subjected to the random excitation can experience the complex nonlinear aperiodic vibration. Displacement bifurcation diagrams show that the change of the stretch ratio of the DE membrane in the length direction during a harvesting cycle can be improved by increasing the upper limiting frequency and decreasing the intensity and the power spectrum density. In addition, the EH performance of the DE pendulum under the random excitation is studied for the different system parameters, such as the mass of the DE pendulum, the load resistance, and the length of the DE membrane. The

average power density and the efficiency voltage are used to evaluate the EH performance. The simulation results show that as the intensity and the power spectrum density increase, the average power density and the efficiency voltage can decrease. With the increase in the upper limiting frequency, the average power density and the efficiency voltage can first increase and then trend gradually to the saturation. In addition, decreasing the mass of the DE pendulum and the length of the DE membrane can contribute to improving both the average power density and the efficiency voltage. The variation of the average power density with the load resistance exhibits the non-monotonic behavior, while the effective voltage can increase with the increase in the load resistance. The results can help better understand ~~better~~ the random dynamic response of the DE pendulum and provide ~~the~~ a guidance for designing the DE pendulum under the random excitation.

References

[1] Chu S, Cui Y, Liu N. The path towards sustainable energy. Nature materials. 2017;16:16.

[2] Wang J, Zhou S, Zhang Z, Yurchenko D. High-performance piezoelectric wind energy harvester with Y-shaped attachments. Energy Conversion and Management. 2019;181:645-52.

[3] Zhao L-C, Zou H-X, Yan G, Liu F-R, Tan T, Zhang W-M, et al. A water-proof magnetically coupled piezoelectric-electromagnetic hybrid wind energy harvester. Applied Energy. 2019;239:735-46.

[4] Siddique ARM, Mahmud S, Heyst BV. A comprehensive review on vibration based micro power generators using electromagnetic and piezoelectric transducer mechanisms. Energy Conversion and Management. 2015;106:728-47.

[5] Zou H-X, Zhao L-C, Gao Q-H, Zuo L, Liu F-R, Tan T, et al. Mechanical modulations for enhancing energy harvesting: Principles, methods and applications. Applied Energy. 2019;255:113871

[6] Fan P, Zhu L, Chen H, Luo B. Energy harvesting from a DE-based soft pendulum. Smart Materials and Structures. 2018;27:115023.

[7] Zhang CL, Lai ZH, Rao XX, Zhang JW, Yurchenko D. Energy harvesting from a novel contact-type dielectric elastomer generator. Energy Conversion and Management. 2020;205:112351.

[8] Bowen C, Arafa M. Energy harvesting technologies for tire pressure monitoring systems. Advanced Energy Materials. 2015;5:1401787.

[9] Maurya D, Kumar P, Khaleghian S, Sriramdas R, Kang MG, Kishore RA, et al. Energy harvesting and strain sensing in smart tire for next generation autonomous vehicles. Applied energy. 2018;232:312-22.

[10] Lagomarsini C, Jean-Mistral C, Monfray S, Sylvestre A. Optimization of an electret-based soft hybrid generator for human body applications. Smart Materials and Structures. 2019;28:104003.

[11] McKay TG, O'Brien BM, Calius EP, Anderson IA. Soft generators using dielectric elastomers. Applied Physics Letters. 2011;98:142903.

[12] Wang X, Niu S, Yi F, Yin Y, Hao C, Dai K, et al. Harvesting ambient vibration energy

over a wide frequency range for self-powered electronics. ACS nano. 2017;11:1728-35.
[13] Ahmed S, Kakkar V. An electret-based angular electrostatic energy harvester for battery-less cardiac and neural implants. IEEE Access. 2017;5:19631-43.
[14] Beker L, Benet A, Meybodi AT, Eovino B, Pisano AP, Lin L. Energy harvesting from cerebrospinal fluid pressure fluctuations for self-powered neural implants. Biomedical microdevices. 2017;19:32.
[15] Huang J, Shian S, Suo Z, Clarke DR. Maximizing the Energy Density of Dielectric Elastomer Generators Using Equi‐Biaxial Loading. Advanced Functional Materials. 2013;23:5056-61.
[16] Panigrahi R, Mishra SK. An Electrical Model of a Dielectric Elastomer Generator. IEEE Transactions on Power Electronics. 2018;33:2792-7.
[17] McKay TG, Rosset S, Anderson IA, Shea H. Dielectric elastomer generators that stack up. Smart Materials and Structures. 2015;24:015014.
[18] Chu B, Zhou X, Ren K, Neese B, Lin M, Wang Q, et al. A dielectric polymer with high electric energy density and fast discharge speed. Science. 2006;313:334-6.
[19] Fan P, Chen H. Effect of crosslinks, entanglements, and chain extensibilities on dynamic electromechanical instability of dielectric elastomers. EPL (Europhysics Letters). 2018;124:37001.
[20] Pelrine R, Kornbluh R, Pei Q, Joseph J. High-speed electrically actuated elastomers with strain greater than 100%. Science. 2000;287:836-9
[21] Fan P, Chen H, Li B, Wang Y. Performance investigation on dissipative dielectric elastomer generators with a triangular energy harvesting scheme. EPL (Europhysics Letters). 2017;120:47007.
[22] Foo CC, Koh SJA, Keplinger C, Kaltseis R, Bauer S, Suo Z. Performance of dissipative dielectric elastomer generators. Journal of Applied Physics. 2012;111:094107.
[23] Zhao Y, Meng G, Zhang W. Characterization and modeling of viscoelastic hysteresis in a dielectric elastomer actuator. Smart Materials and Structures. 2020;29:055019.
[24] Linnebach P, Rizzello G, Seelecke S. Design and validation of a dielectric elastomer membrane actuator driven pneumatic pump. Smart Materials and Structures. 2020
[25] Han M, Lee J, Kim JK, An HK, Kang S-W, Jung D. Highly sensitive and flexible wearable pressure sensor with dielectric elastomer and carbon nanotube electrodes. Sensors and Actuators A: Physical. 2020;305:111941.
[26] Loew P, Brill M, Rizzello G, Seelecke S. Development of a nonintrusive pressure sensor for polymer tubes based on dielectric elastomer membranes. Sensors and Actuators A: Physical. 2019;292:1-10.
[27] Christianson C, Goldberg NN, Deheyn DD, Cai S, Tolley MT. Translucent soft robots driven by frameless fluid electrode dielectric elastomer actuators. Science Robotics. 2018;3:eaat1893.
[28] Shintake J, Cacucciolo V, Shea H, Floreano D. Soft Biomimetic Fish Robot Made of Dielectric Elastomer Actuators. Soft robotics. 2018;5:466-74.
[29] Pelrine R, Kornbluh RD, Eckerle J, Jeuck P, Oh S, Pei Q, et al. Dielectric elastomers: generator mode fundamentals and applications. Proc. SPIE. 2001;4329:148-56.
[30] McMeeking RM, Landis CM. Electrostatic forces and stored energy for deformable dielectric materials. 2005;72:581-90.
[31] Suo Z, Zhao X, Greene W. A nonlinear field theory of deformable dielectrics. Journal of the Mechanics and Physics of Solids. 2008;56:467-86.

[32] York A, Dunn J, Seelecke S. Experimental characterization of the hysteretic and rate-dependent electromechanical behavior of dielectric electro-active polymer actuators. Smart Materials and Structures. 2010;19:094014.
[33] Foo CC, Cai S, Koh SJA, Bauer S, Suo Z. Model of dissipative dielectric elastomers. Journal of Applied Physics. 2012;111:034102.
[34] Lv X, Liu L, Liu Y, Leng J. Dielectric elastomer energy harvesting: maximal converted energy, viscoelastic dissipation and a wave power generator. Smart Materials and Structures. 2015;24:115036.
[35] Zhou J, Jiang L, Khayat RE. Methods to improve harvested energy and conversion efficiency of viscoelastic dielectric elastomer generators. Journal of Applied Physics. 2017;121:184102.
[36] Zhou J, Jiang L, Khayat RE. Investigation on the performance of a viscoelastic dielectric elastomer membrane generator. Soft matter. 2015;11:2983-92.
[37] Fan P, Chen H. Performance investigation of a dissipative dielectric elastomer generator by the damping model. Applied Physics A. 2018;124.
[38] Chen SE, Deng L, He ZC, Li E, Li GY. Temperature effect on the performance of a dissipative dielectric elastomer generator with failure modes. Smart Materials and Structures. 2016;25:055017.
[39] Wang Y, Zhou JX, Wu XH, Li B, Zhang L. Energy Diagrams of Dielectric Elastomer Generators under Different Types of Deformation. Chinese Physics Letters. 2013;30:066103.
[40] Shian S, Huang J, Zhu S, Clarke DR. Optimizing the electrical energy conversion cycle of dielectric elastomer generators. Adv Mater. 2014;26:6617-21.
[41] Chiba S, Waki M, Wada T, Hirakawa Y, Masuda K, Ikoma T. Consistent ocean wave energy harvesting using electroactive polymer (dielectric elastomer) artificial muscle generators. Applied Energy. 2013;104:497-502.
[42] Moretti G, Papini GPR, Righi M, Forehand D, Ingram D, Vertechy R, et al. Resonant wave energy harvester based on dielectric elastomer generator. Smart Materials and Structures. 2018;27:035015.
[43] Yurchenko D, Val DV, Lai ZH, Gu G, Thomson G. Energy harvesting from a DE-based dynamic vibro-impact system. Smart Materials and Structures. 2017;26:105001.
[44] Lai ZH, Wang JL, Zhang CL, Zhang GQ, Yurchenko D. Harvest wind energy from a vibro-impact DEG embedded into a bluff body. Energy Conversion and Management. 2019;199:111993.
[45] Thomson G, Yurchenko D, Val DV, Zhang Z. Predicting energy output of a stochastic nonlinear dielectric elastomer generator. Energy Conversion and Management. 2019;196:1445-52.
[46] Zhang C, Lai Z, Rao X, Zhang J, Yurchenko D. Energy harvesting from a novel contact-type dielectric elastomer generator. Energy Conversion and Management. 2020;205:112351.
[47] Hong W. Modeling viscoelastic dielectrics. Journal of the Mechanics and Physics of Solids. 2011;59:637-50.
[48] Gent AN. A new constitutive relation for rubber. Rubber Chem. Technol. 1996;69:59-61.
[49] Wedig WV. Invariant measures and Lyapunov exponents for generalized parameter fluctuations. Structural Safety. 1990;8:13-25.
[50] Chen LQ, Jiang WA. Internal Resonance Energy Harvesting. Journal of Applied

Mechanics. 2015;82:031004.
[51] Haiwu R, Wei X, Xiangdon W, Guang M, Tong F. Response statistics of two-degree-of-freedom non-linear system to narrow-band random excitation. International journal of non-linear mechanics. 2002;37:1017-28.